

## Linear stability of Poiseuille flow over a steady spanwise Stokes layer

Daniele Massaro <sup>1,2,\*</sup>, Fulvio Martinelli <sup>3</sup>, Peter Schmid<sup>4,†</sup> and Maurizio Quadrio <sup>2,‡</sup>

<sup>1</sup>*SimEx/FLOW, Engineering Mechanics, KTH Royal Institute of Technology, SE-100 44 Stockholm, Sweden*

<sup>2</sup>*Department of Aerospace Sciences and Technologies, Politecnico di Milano,  
via La Masa 34 20156 Milano, Italy*

<sup>3</sup>*Laboratoire d'Hydrodynamique (LadHyX), CNRS-École Polytechnique, F-91128 Palaiseau, France*

<sup>4</sup>*Department of Mechanical Engineering, PSE Division, KAUST, 23955 Thuwal, Saudi Arabia*



(Received 16 April 2023; accepted 19 September 2023; published 9 October 2023)

The temporal linear stability of plane Poiseuille flow modified by spanwise forcing applied at the walls is considered. The forcing consists of a stationary streamwise distribution of spanwise velocity that generates a steady transversal Stokes layer, known to reduce skin-friction drag in a turbulent flow with little energetic cost. A large numerical study is carried out, where the effects of both the physical and the discretization parameters are thoroughly explored, for three representative subcritical values of the Reynolds number  $Re$ . Results show that the spanwise Stokes layer significantly affects the linear stability of the system. For example, at  $Re = 2000$  the wall forcing is found to more than double the negative real part of the least-stable eigenvalue, and to decrease by nearly a factor of 4 the maximum transient growth of perturbation energy. These observations are  $Re$  dependent and further improve at higher  $Re$ . Comments on the physical implications of the obtained results are provided, suggesting that spanwise forcing might be effective to obtain at the same time a delayed transition to turbulence and a reduced turbulent friction.

DOI: [10.1103/PhysRevFluids.8.103902](https://doi.org/10.1103/PhysRevFluids.8.103902)

### I. INTRODUCTION

Decreasing the aerodynamic drag is a formidable scientific and technological challenge in configurations dominated by a relative motion between a solid body and a surrounding fluid. In particular, the skin-friction drag—in the laminar or in the turbulent regime—often represents a major portion of the total drag in the air transport sector, and can be of paramount importance in naval and submarine transport. Skin friction can be reduced either by keeping the flow laminar as long as possible, thus exploiting the intrinsically lower friction levels typical of the laminar regime, or by accepting the transition to turbulence, and reducing the level of turbulent friction below its natural level. A viable flow control approach that achieves both objectives would be very desirable, as it would first take advantage of laminarity as long as possible, and then continue to reduce turbulent friction.

Among the several active techniques for the reduction of turbulent drag, we are interested in spanwise-forcing techniques, and the present paper, in particular, considers streamwise-traveling waves of spanwise wall-velocity as introduced by Quadrio *et al.* (2009) [1]. Comprehensive reviews on this technique for turbulent drag reduction are available [2–4]. The streamwise-traveling waves, which include as a special case the spanwise-oscillating wall [5] but achieve far higher energetic

---

\* [dmassaro@kth.se](mailto:dmassaro@kth.se)

† [peter.schmid@kaust.edu.sa](mailto:peter.schmid@kaust.edu.sa)

‡ [maurizio.quadrio@polimi.it](mailto:maurizio.quadrio@polimi.it)

efficiency, abate the levels of turbulent skin-friction drag with interesting energetic effectiveness, with one energy unit spent on the control saving up to 30 units of pumping energy. Furthermore, recent evidence has shown that spanwise forcing can bring indirect benefits in terms of the reduction of pressure drag [6]; in addition, it may be highly beneficial by interacting with the shock wave over an aerofoil in transonic flow [7] and reducing significantly the aerodynamic drag of the entire airplane with negligible energy expenditure. Within this context, the present paper is motivated by the following simple question: Can spanwise forcing favorably affect transition to turbulence? Since the forcing is known to weaken near-wall streaks in a turbulent flow [8], a similar effect on laminar streaks might alter their growth, thus causing a delay of, or perhaps preventing altogether, transition to turbulence. It must be kept in mind that, at the moment, satisfactory actuators for implementing traveling waves in a real-world application are still lacking, even though some interesting developments exist, including mechanical movement of the wall [9,10], electroactive polymers [11,12], and the use of Kagome lattices [13]. However, the prospect of instrumenting, e.g., an airplane wing with one actuator that, in the wing fore part, would delay transition while, in the aft, would decrease turbulent skin-friction drag is certainly appealing, and motivates further research efforts into this direction.

This paper is not the first to investigate the stability properties of a wall-bounded flow modified by spanwise forcing, and the available body of literature provides important guidance. Most of the current knowledge concerns spatially uniform wall oscillations. Jovanović (2008) [14] demonstrated the capability of properly designed wall oscillations to reduce receptivity of the linearized Navier-Stokes (NS) equations to small stochastic disturbances in laminar Poiseuille flow. Ricco (2011) [15] showed in a linearized study that a substantial reduction in the intensity of laminar streaks under steady spatial oscillations is possible, with reductions up to 90% of the peak value of velocity fluctuations. Rabin *et al.* (2014) [16] studied plane Couette flow under spatially uniform wall oscillations: By solving a fully nonlinear problem, they demonstrated and quantified how the critical disturbance energy required for the onset of turbulence increases due to spanwise forcing. Hack and Zaki (2012) [17], using a linearized analysis of temporal harmonic wall oscillations, provided further evidence for near-wall shear filtering as an effective tool. In a followup study [18], the influence of spanwise forcing on by-pass transition in the boundary layer over a flat plate was examined. They found that oscillations, when properly tuned, can substantially delay transition, with overall energy gains. This DNS-based study was later corroborated by a corresponding Floquet stability analysis [19], where the changes in the linear modal and nonmodal instability mechanisms operating in the pretransitional boundary layer induced by the spanwise forcing were studied. This investigation confirmed important stabilization mechanisms due to weaker nonmodal growth, but found that transition is enhanced, owing to a reinforcement of modal instabilities, at larger forcing amplitudes. Similarly, Wang and Liu (2019) [20] found that spanwise oscillations of the wall can act as precursors to the transition process in a boundary layer.

For the spatially varying case, where no stability study is presently available, Duque-Daza *et al.* (2012) [21] numerically solved a linearized version of the NS equations for a plane channel setting to investigate how streamwise-traveling waves impact the growth of near-wall low-speed streaks. They found that the computed relative change in streak amplification due to traveling waves varies with the parameters defining the wave in a way that strictly resembles the DNS-measured drag reduction data in the turbulent regime. Negi *et al.* (2015) [22] simulated via DNS a single low-speed streak forced by a standing wave of spanwise wall forcing in the laminar regime, and found that the skin friction can drop below the laminar reference value. They also reported a delay in the characteristic rise of skin friction during transition. Negi *et al.* (2019) [23] used large-eddy simulations to study bypass transition in a spatially evolving boundary layer. Temporal and spatial oscillations of the wall forcing were considered, and transition delay could be observed in both cases. A qualitative explanation was offered, attributing the transition delay to the additional filtering of the disturbance by the Stokes layer. An optimum forcing amplitude for transition delay was identified,

while acknowledging that at larger wavelengths the delay appears to increase monotonically with amplitude.

Motivated by the above studies, this paper focuses on plane channel flow as a model problem and studies the modal and nonmodal stability of the laminar, pressure-driven Poiseuille flow modified by streamwise-distributed spanwise forcing in the form of a steady Stokes layer (SSL) [24]. The SSL is created by a (spanwise-uniform) stationary spanwise velocity at the wall that is sinusoidally distributed along the streamwise direction. The streamwise-varying base flow prohibits the direct application of a classic Orr–Sommerfeld–Squire (OSS) linear stability analysis, since the resulting system of differential equations contains streamwise-varying coefficients and thus requires a global approach. Here, extending an approach introduced by Floryan and coworkers [25,26], we exploit the particular form of the base flow to avoid a global stability analysis. The study is conceptually close to a classical secondary instability analysis, in which finite amplitude disturbances saturate and establish a new base flow, whose linear stability is then studied [27]; in the present case, it is the superimposed sinusoidal spanwise flow that alters the Poiseuille streamwise base flow.

The structure of this paper is as follows. In Sec. II, the mathematical formulation is presented, emphasizing analogies and differences with respect to a classic OSS analysis; the numerical tools are validated against direct numerical simulations. Next, in Sec. III the physical parameters of the problem are discussed (the discussion of the discretization-related parameters is deferred to Appendix A), and the computational procedures employed in the execution of a large parameter study are described. In Sec. IV, the main results of the modal and nonmodal stability analysis are discussed, and concluding remarks are offered in Sec. V, together with a critical discussion of the main findings.

## II. MATHEMATICAL FORMULATION

This section describes the setup of the linear stability analysis, based on the well-known OSS problem for Poiseuille flow augmented by terms that model the presence of a spanwise base flow induced by the forcing.

The governing equations are the incompressible NS equations, which in nondimensional form read

$$\begin{aligned} \nabla \cdot \mathbf{V} &= 0 \\ \frac{\partial \mathbf{V}}{\partial t} + (\mathbf{V} \cdot \nabla) \mathbf{V} &= -\nabla P + \frac{1}{\text{Re}} \nabla^2 \mathbf{V}, \end{aligned} \quad (1)$$

where  $\mathbf{V}$  is the nondimensional velocity field,  $P$  is the nondimensional pressure, and  $\text{Re}$  denotes the Reynolds number, defined with the kinematic viscosity  $\nu$  of the fluid, the length scale  $h$ , in our case the channel half-height, and the velocity scale  $U_c$ , in our case the centerline velocity of the laminar Poiseuille profile. The length and velocity scales  $h$  and  $U_c$  are used to express any quantity in dimensionless form. The NS equations are then expressed in a Cartesian coordinate system for the plane channel flow, with  $x, y, z$  (and  $U, V, W$ ) indicating the streamwise, wall-normal, and spanwise directions (and corresponding velocity components). A sketch of the flow with the employed reference system is shown in Fig. 1.

The boundary conditions for the velocity at the wall are  $U = 0$  and  $V = 0$ , but, in contrast to standard Poiseuille flow, the spanwise component is nonzero. Within the general class of streamwise-traveling waves [1], the purely spatially modulated standing wave considered by Viotti *et al.* (2009) [24] is considered, so the wall forcing applied at both walls is

$$W(x) = A \cos(\kappa x), \quad (2)$$

where  $A$  denotes the maximum forcing amplitude and  $\kappa$  stands for the forcing wave number.

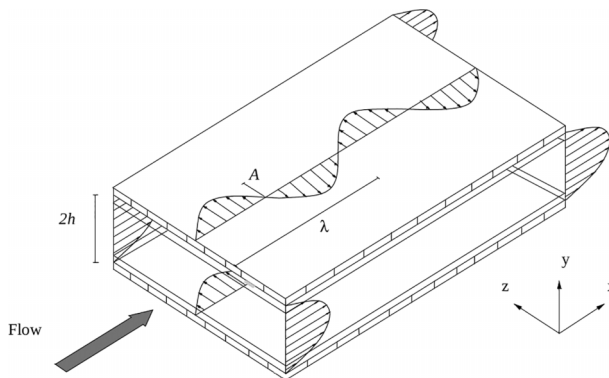


FIG. 1. Sketch of plane channel with the chosen reference system. The two channel walls are separated by a distance  $2h$ ; a stationary wall forcing is applied at both walls, and is characterized by its wavelength  $\lambda$  and maximum velocity amplitude  $A$ .

### A. The base flow

It was shown by Viotti *et al.* (2009) [24] (and later by Quadrio and Ricco (2011) [28] in the wider context of traveling-wave forcing) that in the laminar regime the spanwise wall-velocity does not affect the streamwise flow, which still follows the parabolic Poiseuille solution but creates a wall-normal distribution of spanwise velocity. Hence, the base flow (indicated with an overbar) in the streamwise direction  $\bar{U}(y) = 1 - y^2$  is identical to the no-forcing case  $A = 0$ , whereas the spanwise base flow  $\bar{W}(x, y)$ , unaffected by the streamwise flow, corresponds to  $\text{Re} = 0$ ; it is computed from the spanwise component of the momentum equation,

$$(1 - y^2) \frac{\partial W}{\partial x} = \frac{1}{\text{Re}} \left( \frac{\partial^2 W}{\partial x^2} + \frac{\partial^2 W}{\partial y^2} \right), \quad (3)$$

with the nondimensional boundary condition

$$W(x, \pm 1, z, t) = \frac{A}{2} (e^{j\kappa x} + e^{-j\kappa x}), \quad (4)$$

where  $j$  is the imaginary unit. Equation (3) is linear with streamwise-constant coefficients. By enforcing periodicity and using separation of variables, the  $W$  base flow has the form

$$\bar{W}(x, y) = \text{Re}\{f(y)e^{j\kappa x}\} = \frac{1}{2}(f(y)e^{j\kappa x} + f^*(y)e^{-j\kappa x}), \quad (5)$$

where  $\text{Re}$  indicates the real part of a complex quantity and the asterisk indicates complex conjugation. The function  $f(y)$  is computed numerically from the following parabolic cylinder equation, obtained by substituting Eq. (5) into Eq. (3) with  $f(\pm 1) = A$ :

$$f''(y) - \kappa[\kappa + j\text{Re}(1 - y^2)]f(y) = 0. \quad (6)$$

Under the hypothesis that the thickness of the transverse Stokes layer is small compared to  $h$ , and that streamwise diffusion is negligible with respect to the wall-normal diffusion, Viotti *et al.* (2009) [24] determined the following solution:

$$f(y) = \text{Ai}\left(-e^{-j\frac{4}{3}\pi} jy/\delta_x\right),$$

in which  $\text{Ai}$  represents the Airy function [29] and  $\delta_x = (\nu/\kappa u_{y,0})^{1/3}$  is a representative wall-normal scale of the SSL, defined in terms of the fluid viscosity  $\nu$ , the forcing wave number  $\kappa$ , and the longitudinal wall shear  $u_{y,0}$ .

### B. Linearized equations for the perturbations

Our interest lies on the dynamics of small perturbations  $u, v, w, p$  to the base flow. After substituting the following decompositions:

$$U = \bar{U} + u, \quad V = v, \quad W = \bar{W} + w, \quad P = \bar{P} + p, \quad (7)$$

into the NS Eq. (1), and subtracting the base flow equations from the linearized perturbation equations, obtained by dropping the quadratic terms in the small perturbations, one obtains

$$\begin{aligned} u_x + v_y + w_z &= 0 \\ u_t + \bar{U}u_x + v\bar{U}' + \bar{W}u_z &= -p_x + \frac{1}{\text{Re}}\nabla^2 u \\ v_t + \bar{U}v_x + \bar{W}v_z &= -p_y + \frac{1}{\text{Re}}\nabla^2 v \\ w_t + \bar{U}w_x + u\bar{W}_x + v\bar{W}_y + \bar{W}w_z &= -p_z + \frac{1}{\text{Re}}\nabla^2 w, \end{aligned} \quad (8)$$

where the prime indicates the wall-normal derivative.

### C. The $v - \eta$ formulation

The usual steps leading to the OSS equations [27] can be followed here to obtain a compact expression of the linear dynamics, under the incompressibility constraint, in terms of two evolution equations for the wall-normal components  $v$  and  $\eta = \partial u/\partial z - \partial w/\partial x$  of the perturbation velocity and vorticity vectors, respectively. The former equation reads

$$\begin{aligned} \frac{\partial}{\partial t}\nabla^2 v + \left(\bar{U}\frac{\partial}{\partial x} + \bar{W}\frac{\partial}{\partial z}\right)\nabla^2 v - \left(\bar{U}''\frac{\partial}{\partial x} + \bar{W}_{yy}\frac{\partial}{\partial z}\right)v \\ - 2\bar{W}_{xy}u_z - 2\bar{W}_x\frac{\partial}{\partial z}(u_y - v_x) + \bar{W}_{xx}v_z = \frac{1}{\text{Re}}\nabla^2\nabla^2 v, \end{aligned} \quad (9)$$

while the latter equation can be stated as

$$\frac{\partial}{\partial t}\eta + \left(\bar{U}\frac{\partial}{\partial x} + \bar{W}\frac{\partial}{\partial z}\right)\eta + \left(\bar{W}_x\frac{\partial}{\partial y} + \bar{U}'\frac{\partial}{\partial z} - \bar{W}_{xy} - \bar{W}_y\frac{\partial}{\partial x}\right)v - u\bar{W}_{xx} = \frac{1}{\text{Re}}\nabla^2\eta, \quad (10)$$

with boundary conditions of the form

$$v(\pm 1) = 0; \quad \eta(\pm 1) = 0; \quad \frac{\partial v}{\partial y}(\pm 1) = 0. \quad (11)$$

As in the standard case, these two equations are complemented by a differential system which relates  $u$  and  $w$  to  $v$  and  $\eta$  via the continuity equation and the definition of the wall-normal vorticity. In contrast to the no-forcing OSS case, the two equations are fully coupled via  $\bar{W}$ , and several coefficients are varying along the streamwise direction.

### D. Fourier transform

The standard OSS system is conveniently Fourier-transformed along the two homogeneous wall-parallel directions. In our case, this step can be straightforwardly applied in the spanwise  $z$  direction, giving rise to an expansion with spanwise wave number  $\beta$ , since Eqs. (9) and (10) consist of  $z$ -independent coefficients. The coefficients' streamwise dependence in Eqs. (9) and (10) prevents a straightforward Fourier transform in that direction. However, their functional variation is not generic, as it derives from the functional form of the base flow Eq. (5) only; hence the coefficients must be harmonic functions of  $x$  with wave number  $\kappa$ . We follow an approach introduced in Ref. [25] for the study of the stability of a parallel wall flow modified by periodic blowing and suction, and

leverage the sinusoidal variation of the base flow. The flow variables are expanded in a (finite) Fourier series along the streamwise direction as

$$\check{v}(x, y, t; \beta) = \sum_{i=-M}^{+M} \hat{v}_i(y, t; \beta) e^{j(m+i)\kappa x}; \quad \check{\eta}(x, y, t; \beta) = \sum_{i=-M}^{+M} \hat{\eta}_i(y, t; \beta) e^{j(m+i)\kappa x}, \quad (12)$$

with  $M$  as the degree of the spectral expansion of the flow variables,  $i$  as an integer index, and  $m \in [0, 1)$  as a real number defining the actual expansion wave number  $\alpha = (m + i)\kappa$ . The parameter  $m$  is referred to as the detuning parameter, since it is used to detune the perturbation against the base flow. In this preliminary work, we set  $m = 0$ . Note that Ref. [25] considered  $M = 3$ , whereas in this paper  $M$  is much larger and, like the other discretization parameters, is dynamically adapted to each case after a sensitivity analysis. The procedure for setting the discretization parameters is described in Appendix A.

Equations (9) and (10) can now be Fourier transformed along the  $x$  direction, introducing the streamwise wave number  $\tilde{\alpha}$  in the process. A generic  $x$ -dependent term  $q(x)$  is Fourier transformed as follows:

$$\hat{q}(\tilde{\alpha}) = \frac{\kappa}{2\pi} \int_0^{2\pi/\kappa} q(x) e^{-j\tilde{\alpha}x} dx.$$

Since in Eqs. (9) and (10), terms with complex exponentials are of the kind  $e^{j\alpha x}$  and  $e^{\pm j\kappa x} e^{j\alpha x}$ , Fourier-transforming in the  $x$  direction leads to integrals of the following general form:

$$\int_0^{2\pi/\kappa} e^{\pm j\kappa x} e^{j\alpha x} e^{-j\tilde{\alpha}x} dx.$$

Owing to the orthogonality of the trigonometric functions, they are proportional to  $\delta_{\tilde{\alpha}, \pm\kappa + \alpha}$ , i.e., they are always zero unless  $\alpha = \tilde{\alpha} \mp \kappa$ . By introducing the operator  $\tilde{\Delta} = \partial^2/\partial y^2 - \tilde{\alpha}^2 - \beta^2$ , the equation governing the evolution of  $\hat{\eta}_{\tilde{\alpha}} \equiv \hat{\eta}(y, t; \tilde{\alpha}, \beta)$  is

$$\begin{aligned} \frac{\partial}{\partial t} \hat{\eta}_{\tilde{\alpha}} &= -j\tilde{\alpha}\bar{U}\hat{\eta}_{\tilde{\alpha}} - j\beta\bar{U}'\hat{v}_{\tilde{\alpha}} + \frac{1}{\text{Re}} \tilde{\Delta}\hat{\eta}_{\tilde{\alpha}} - \frac{j\beta}{2} f \left( 1 - \frac{\kappa^2}{(\tilde{\alpha} - \kappa)^2 + \beta^2} \right) \hat{\eta}_{\tilde{\alpha} - \kappa} \\ &+ \frac{j\beta}{2} f^* \left[ 1 - \frac{\kappa^2}{(\tilde{\alpha} + \kappa)^2 + \beta^2} \right] \hat{\eta}_{\tilde{\alpha} + \kappa} - \frac{j}{2} \left[ \kappa f \left( 1 + \frac{\kappa(\tilde{\alpha} - \kappa)}{(\tilde{\alpha} - \kappa)^2 + \beta^2} \right) \frac{\partial}{\partial y} - f' \tilde{\alpha} \right] \hat{v}_{\tilde{\alpha} - \kappa} \\ &+ \frac{j}{2} \left[ \kappa f^* \left( 1 - \frac{\kappa(\tilde{\alpha} + \kappa)}{(\tilde{\alpha} + \kappa)^2 + \beta^2} \right) \frac{\partial}{\partial y} + f^{*\prime} \tilde{\alpha} \right] \hat{v}_{\tilde{\alpha} + \kappa} \end{aligned} \quad (13)$$

Analogously, the equation for  $\hat{v}_{\tilde{\alpha}} \equiv \hat{v}(y, t; \tilde{\alpha}, \beta)$  reads

$$\begin{aligned} \frac{\partial}{\partial t} \tilde{\Delta}\hat{v}_{\tilde{\alpha}} &= -j\tilde{\alpha}\bar{U}\tilde{\Delta}\hat{v}_{\tilde{\alpha}} + j\tilde{\alpha}\bar{U}''\hat{v}_{\tilde{\alpha}} + \frac{1}{\text{Re}} \tilde{\Delta}\tilde{\Delta}\hat{v}_{\tilde{\alpha}} \\ &+ \frac{j\beta^2\kappa}{(\tilde{\alpha} - \kappa)^2 + \beta^2} \left( f' + f \frac{\partial}{\partial y} \right) \hat{\eta}_{\tilde{\alpha} - \kappa} - \frac{j\beta^2\kappa}{(\tilde{\alpha} + \kappa)^2 + \beta^2} \left( f^{*\prime} + f^* \frac{\partial}{\partial y} \right) \hat{\eta}_{\tilde{\alpha} + \kappa} \\ &- \frac{j\beta}{2} \left[ f\tilde{\Delta}_- - f'' - \kappa f(2\tilde{\alpha} - \kappa) + 2 \frac{\kappa(\tilde{\alpha} - \kappa)}{(\tilde{\alpha} - \kappa)^2 + \beta^2} \left( f' \frac{\partial}{\partial y} + f \frac{\partial^2}{\partial y^2} \right) \right] \hat{v}_{\tilde{\alpha} - \kappa} \\ &- \frac{j\beta}{2} \left[ f^*\tilde{\Delta}_+ - f^{*\prime} + \kappa f^*(2\tilde{\alpha} + \kappa) - 2 \frac{\kappa(\tilde{\alpha} + \kappa)}{(\tilde{\alpha} + \kappa)^2 + \beta^2} \left( f^{*\prime} \frac{\partial}{\partial y} + f^* \frac{\partial^2}{\partial y^2} \right) \right] \hat{v}_{\tilde{\alpha} + \kappa}, \end{aligned} \quad (14)$$

where  $\tilde{\Delta}_{\pm} = \partial^2/\partial y^2 - (\tilde{\alpha} \pm \kappa)^2 - \beta^2$ .

When compared to the standard OSS problem, Eqs. (13) and (14) contain several additional terms related to the spanwise base flow, described by the function  $f(y)$ . Terms containing  $\hat{v}$  and  $\hat{\eta}$  evaluated at  $\tilde{\alpha}$  are identical to the OSS equations, whereas the remaining terms represent effects of disturbances at wave numbers  $\tilde{\alpha} \pm \kappa$ .

FIG. 2. Graphical representation of the system  $\dot{\mathbf{q}} = \mathbf{A}_s \mathbf{q}$ . The matrix is block tridiagonal with block size  $M \times M$ . The red blocks on the diagonal correspond to the classic OSS matrices for each streamwise wave number, whereas the adjacent green and yellow blocks describe interactions with contiguous streamwise wave numbers.

### E. Numerical discretization

From here on, a change in notation is introduced. In fact, the governing Eqs. (13) and (14) can be equivalently derived by substituting the modal expansions Eqs. (12) into the  $v$ - $\eta$  equations and by Fourier transforming against a testing function of the form  $e^{j(p+m)\kappa}$ , where  $p \in [-M, M]$  is an integer such that  $\tilde{\alpha} = (p + m)\kappa$ .

Starting from this form, the  $y$ -dependent terms are discretized via Chebyshev polynomials on a grid of Gauss-Lobatto nodes [30–32]. The unknown  $\hat{v}_p$  is thus written as

$$\hat{v}_p(y) = \sum_{n=0}^N v_{p,n} T_n(y) \quad (15)$$

or, in matrix form,  $\hat{\mathbf{v}}_p = \mathbf{D}_0 \mathbf{v}_p$ , with  $\mathbf{D}_0$  as a square  $(N + 1) \times (N + 1)$  matrix. Similar matrices  $\mathbf{D}_1$ ,  $\mathbf{D}_2$ , and  $\mathbf{D}_4$  represent the first, second, and fourth derivative.

For a given  $p$ , Eqs. (13) and (14) can be written compactly in the following block form:

$$\frac{\partial}{\partial t} \underbrace{\begin{bmatrix} B_{11} & 0 \\ 0 & B_{22} \end{bmatrix}}_{\mathbf{B}^{(p)}} \begin{pmatrix} v \\ \eta \end{pmatrix}_p = \underbrace{\begin{bmatrix} L_{m11} & L_{m12} \\ L_{m21} & L_{m22} \end{bmatrix}}_{\mathbf{L}^{(p)}} \begin{pmatrix} v \\ \eta \end{pmatrix}_{p-1} + \underbrace{\begin{bmatrix} L_{11} & 0 \\ L_{21} & L_{22} \end{bmatrix}}_{\mathbf{L}^{(p)}} \begin{pmatrix} v \\ \eta \end{pmatrix}_p + \underbrace{\begin{bmatrix} L_{p11} & L_{p12} \\ L_{p21} & L_{p22} \end{bmatrix}}_{\mathbf{L}_+^{(p)}} \begin{pmatrix} v \\ \eta \end{pmatrix}_{p+1}, \quad (16)$$

where  $\mathbf{B}^{(p)}$  is a diagonal matrix,  $\mathbf{L}^{(p)}$  describes the interaction of  $v$  and  $\eta$ , for a given wave number  $\tilde{\alpha}$ , with themselves (red blocks in Fig. 2);  $\mathbf{L}_-^{(p)}$  and  $\mathbf{L}_+^{(p)}$  (green and yellow blocks in Fig. 2) describe the interactions with the previous and subsequent streamwise wave numbers, respectively, and contain the effect of the spanwise base flow.

Equation (16) must be solved for all  $p$  of the truncated modal expansion  $[-M, +M]$ . Therefore, after grouping the unknowns  $v$  and  $\eta$  into a single array of unknowns  $\mathbf{q}$ , one obtains the following block form:

$$\frac{\partial}{\partial t} (\mathbf{B}_s \mathbf{q}) = \mathbf{L}_s \mathbf{q}, \quad \dot{\mathbf{q}} = \mathbf{B}_s^{-1} \mathbf{L}_s \mathbf{q} = \mathbf{A}_s \mathbf{q} \quad (17)$$

where  $\mathbf{q}$  is a vector composed of  $(N + 1)$  pairs of  $v$ - $\eta$  components, each at a different  $p$  value, so with dimension  $(2M + 1)2(N + 1)$ ;  $\mathbf{B}_s$  and  $\mathbf{L}_s$  are block-tridiagonal square matrices, whose dimensions are  $(2M + 1)2(N + 1) \times (2M + 1)2(N + 1)$ . The structure of the system matrix  $\mathbf{A}_s$  is shown in Fig. 2, which emphasizes its block-tridiagonal structure, with block size  $M \times M$ .

The boundary conditions Eqs. (11) at the two walls are rewritten as

$$\hat{v}_p(\pm 1) = 0; \quad \hat{\eta}_p(\pm 1) = 0; \quad \frac{\partial \hat{v}_p}{\partial y}(\pm 1) = 0. \quad (18)$$

They are readily enforced via appropriate modifications of the matrices  $\mathbf{B}^{(p)}$ ,  $\mathbf{L}^{(p)}$ ,  $\mathbf{L}_-^{(p)}$ , and  $\mathbf{L}_+^{(p)}$ . Following Ref. [27], the boundary values for  $\hat{v}_p$  and  $\hat{\eta}_p$  are set not to exact zero, but to a very small value, i.e.,  $10^{-6}$ ; the extremely fast dynamics associated to this nonzero value does not interfere with the flow dynamics, but the accuracy in computing eigenvalues is improved as the spurious modes associated to the discrete boundary condition are mapped far away in the complex plane.

### F. Modal and nonmodal stability characteristics

In what follows, the modal stability of the system will be assessed by computing the eigenvalues of the system matrix  $\mathbf{A}_s$  which describes the linearized dynamics of the system. Due to the size and sparsity of the matrix, its eigenvalues are most efficiently computed with the Arnoldi method [33]. The number of eigenvalues totals  $N_{\text{tot}} = 2(N + 1) \times (2M + 1)$ , but only a modest fraction of them is of interest here, hence only a subset  $n_{\text{eig}} \ll N_{\text{tot}}$  is computed. This is achieved by a truncation operator  $\mathbf{T}$ , a matrix with dimensions  $n_{\text{eig}} \times N_{\text{tot}}$ . The relation  $\mathbf{q} = \mathbf{T}\mathbf{x}$  transforms Eqs. (17) as

$$\dot{\mathbf{x}} = \mathbf{T}^{-1}\mathbf{A}_s\mathbf{T}\mathbf{x} = \mathbf{\Lambda}\mathbf{x}, \quad (19)$$

where  $\mathbf{\Lambda}$  is a diagonal matrix containing the  $n_{\text{eig}}$  computed eigenvalues and  $\mathbf{T}$  contains the corresponding eigenvectors.

While computing the largest eigenvalue would, in principle, suffice for deciding on modal stability or instability, choosing the right size of the truncation operator is essential in studying the nonmodal stability of the flow (see, e.g., Refs. [27,34,35]). The kinetic energy density  $e$  of an infinitesimal perturbation for a given  $p$  is written as

$$e(p, \beta, t) = \frac{1}{2} \left( \frac{1}{2k^2} \int_{-1}^1 \hat{\mathbf{q}}_p^H \begin{bmatrix} k^2 + D_1^2 & 0 \\ 0 & 1 \end{bmatrix} \hat{\mathbf{q}}_p dy \right), \quad (20)$$

with  $k^2 = \tilde{\alpha}^2 + \beta^2$ ; the superscript  $H$  stands for Hermitian, i.e., the complex conjugate transpose.

After a Chebyshev expansion of  $\mathbf{q}_p$  and after computing the integral weights using the Clenshaw-Curtis quadrature formula [36–39], one obtains

$$e(p, \beta, t) = \begin{pmatrix} \hat{v}_p \\ \hat{\eta}_p \end{pmatrix}^H \underbrace{\left( \frac{1}{4k^2} \begin{bmatrix} k^2 \mathbf{D}_0^H \mathbf{W} \mathbf{D}_0 + \mathbf{D}_1 \mathbf{W} \mathbf{D}_1 & \mathbf{0} \\ \mathbf{0} & \mathbf{D}_0^H \mathbf{W} \mathbf{D}_0 \end{bmatrix} \right)}_{\mathbf{Q}^{(p)}} \begin{pmatrix} \hat{v}_p \\ \hat{\eta}_p \end{pmatrix}, \quad (21)$$

where  $\mathbf{W}$  is a diagonal matrix containing the integral weights, and  $\mathbf{Q}^{(p)}$  represents the energy weight matrix.

Once the full modal expansion  $p \in [-M, M]$  is considered, the square of the energy norm of  $\mathbf{q}$  becomes

$$\|\mathbf{q}(t)\|_E^2 = \mathbf{q}^H \mathbf{Q}_s \mathbf{q},$$

where  $\mathbf{Q}_s$  is the block-diagonal positive definite energy weight matrix for all indices  $p$  in the modal expansion. The energy norm can be rewritten using the truncation operator  $\mathbf{T}$ ,

$$\|\mathbf{q}(t)\|_E^2 = \mathbf{x}^H \mathbf{T}^H \mathbf{Q}_s \mathbf{T} \mathbf{x} = \mathbf{x}^H \tilde{\mathbf{Q}} \mathbf{x},$$

where  $\tilde{\mathbf{Q}} = \mathbf{T}^H \mathbf{Q}_s \mathbf{T}$  can be further decomposed via a Cholesky decomposition  $\tilde{\mathbf{Q}} = \tilde{\mathbf{C}}^H \tilde{\mathbf{C}}$  to result in

$$\|\mathbf{q}(t)\|_E^2 = \|\tilde{\mathbf{C}}\mathbf{x}(t)\|_2^2.$$

The transient energy growth eventually becomes

$$G(t) = \max_{\mathbf{q}_0 \neq \mathbf{0}} \frac{\|\mathbf{q}(t)\|_E^2}{\|\mathbf{q}_0\|_E^2} = \max_{\mathbf{x}_0 \neq \mathbf{0}} \frac{\|\tilde{\mathbf{C}}e^{\mathbf{\Lambda}t}\mathbf{x}_0\|_2^2}{\|\tilde{\mathbf{C}}\mathbf{x}_0\|_2^2} = \|\tilde{\mathbf{C}}e^{\mathbf{\Lambda}t}\tilde{\mathbf{C}}^{-1}\|_2^2. \quad (22)$$

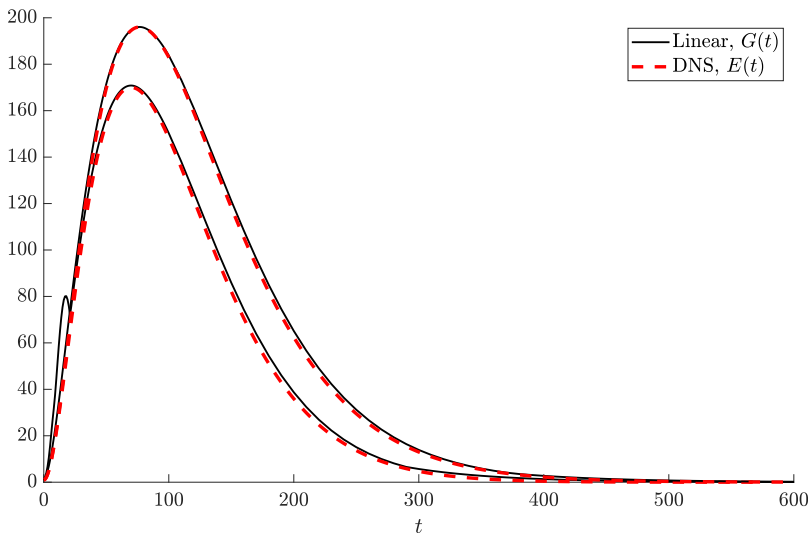


FIG. 3. Comparison between the transient energy growth function  $G(t)$  computed by the linear code (black continuous line) and the DNS-computed temporal evolution of the perturbation energy  $E(t)$  (red dashed line). Reference conditions are  $\text{Re} = 1000$ ,  $\kappa = 1$ , and  $\beta = 2$ . The higher pair of curves corresponds to  $A = 0$  (no control) and the lower one to  $A = 0.1$ .

Lastly, the spatial shape of the optimal perturbation  $\hat{\mathbf{q}}_{\text{in}}$ , and the corresponding spatial shape at the time of the largest energy growth  $\hat{\mathbf{q}}_{\text{out}}$ , are given by

$$\hat{\mathbf{q}}_{\text{in}} = \mathbf{D}_0 \mathbf{T} \bar{\mathbf{C}}^{-1} \mathbf{v}_1, \quad \hat{\mathbf{q}}_{\text{out}} = \mathbf{D}_0 \mathbf{T} \bar{\mathbf{C}}^{-1} \mathbf{u}_1, \quad (23)$$

where  $\mathbf{v}_1$  and  $\mathbf{u}_1$  are the first right and left singular vectors of the matrix  $\bar{\mathbf{C}}e^{\mathbf{A}t}\bar{\mathbf{C}}^{-1}$ , respectively.

### G. Validation

The MATLAB numerical toolkit developed for the stability analysis is first validated against the results of a nonlinear DNS solver. The code, introduced in Ref. [40], where full details are available, solves the incompressible NS equations with mixed spatial discretization, with Fourier expansions in the homogeneous directions (where the pseudospectral approach is used) and compact, fourth-order explicit finite-difference schemes in the wall-normal direction.

The transient energy growth function  $G(t)$  computed by the stability code is compared with the DNS-computed temporal evolution of the energy  $E(t)$  of the optimal initial condition. The test is carried out for  $\text{Re} = 1000$ ,  $\kappa = 1$ ,  $\beta = 2$ . According to the discretization criteria described later in Sec. III and Appendix A, the discretization parameters are set to  $N = 80$ ,  $M = 10$ , and  $A = 0$  or  $A = 0.1$ . The DNS is carried out with 101 points in the wall-normal direction, 32 Fourier modes in the streamwise direction, and 16 modes in the spanwise direction; the size of the temporal step is computed via the Courant-Friedrich-Lewy (CFL) condition by enforcing  $\text{CFL}_{\text{max}} = 0.1$ ; it is verified that the outcome of the DNS is insensitive to further refinements in the temporal and/or spatial discretizations. The initial field for the DNS is made by the base flow, to which the optimal initial condition obtained by the nonmodal stability code is added, after rescaling the amplitude to remain within the limits of linearity. Figure 3 compares the temporal history  $E(t)$  of the DNS-computed energy with the transient growth function  $G(t)$  for the uncontrolled and controlled cases. It can be observed that, as required by their definition,  $G(t) \geq E(t)$  at all times; the two functions coincide at time  $t = t_{G_{\text{max}}}$ . The controlled case with this particular choice of parameters exhibits a reduced maximum transient growth.

### III. PARAMETERS AND COMPUTATIONAL PROCEDURES

The present multiparameter study considers the effects of the following nine parameters, either physical or related to the discretization of the problem:

- (1)  $Re$ , the Reynolds number of the flow
- (2)  $A$ , the maximum amplitude of the wall forcing in Eq. (2)
- (3)  $\kappa$ , the streamwise wave number of the wall forcing in Eq. (2)
- (4)  $\beta$ , the spanwise wave number of the perturbation
- (5)  $N$ , the number of Chebyshev polynomials in Eq. (15)
- (6)  $M$ , the truncation factor in the modal expansion Eqs. (12)
- (7)  $n_{\text{eig}}$ , the number of eigenvalues retained in the Arnoldi algorithm after truncation
- (8)  $\Delta t$ , the temporal step for the discrete evaluation of  $G(t)$
- (9)  $T_{\text{end}}$ , the time at which the computation of  $G(t)$  is stopped

The first four parameters listed above are of a physical nature, and their range defines the breadth of the paper. The remaining parameters are discretization parameters which impact the reliability of the results and the computational cost of the study. The vast range of explored physical parameters, together with the anticipated variable behavior of the system within it, requires efficiency and sensitivity considerations with regard to the chosen discretization.

Description of the choice of discretization parameters is deferred to Appendix A. As far as the physical parameters are concerned, only three subcritical values of the Reynolds number are considered in this paper, namely  $Re = 500$ ,  $Re = 1000$ , and  $Re = 2000$ . The wall forcing is defined by two parameters: its dimensionless amplitude  $A$  is varied between 0 and 1 in increments of 0.1 (resulting in 11 values) and its dimensionless wave number  $\kappa$  is varied between 0.5 and 5 in increments of 0.25 (yielding 19 values). The spanwise wave number  $\beta$  is varied between 0 and 5, with 18 nonequispaced values specifically selected to focus on the most interesting regions. Note that  $\beta = 0$  corresponds to the most unstable two-dimensional waves predicted by the modal theory.  $A = 1$  implies a maximum spanwise velocity equal to the centerline Poiseuille velocity, and  $\kappa = 1$  implies a forcing wavelength that is  $\pi$  times the channel height. Overall, 11 286 cases are computed. The total computational cost is thus considerable, and exceeds 10 000 core hours; a workstation equipped with an Intel i7 CPU with 6 cores has been used.

### IV. RESULTS

#### A. Modal stability

The modal stability characteristics of the flow are evaluated in terms of the real part of the least stable eigenvalue  $\lambda_1$  of the system matrix  $\mathbf{A}_s$ . The effect of wall forcing, represented through the physical parameters  $Re$ ,  $\kappa$ ,  $A$ , and  $\beta$ , on the modal stability properties is quantified via the attenuation-rate increase, expressed via the ratio  $R_{\text{mod}}$ , defined as

$$R_{\text{mod}} = \frac{\text{Re}(\lambda_1)}{\text{Re}(\lambda_1^{\text{ref}})},$$

where  $\lambda_1^{\text{ref}}$  is the least-stable eigenvalue of the unforced Poiseuille flow. Since the considered  $Re$  numbers are subcritical,  $\text{Re}(\lambda_1^{\text{ref}}) < 0$ , and a positive effect of the forcing in the direction of increased stability margin implies  $R_{\text{mod}} > 1$ , in analogy with the drag reduction rate used in the turbulent case to assess the effectiveness of the forcing. The discretization parameters are set according to the criteria described in Appendix A.

For the various values of  $Re$ , Table I reports the values of  $A$ ,  $\beta$ , and  $\kappa$  which have been found to yield the largest increase of  $R_{\text{mod}}$ . The results are  $Re$  dependent, with  $R_{\text{mod}}$  going from 1.9380 at  $Re = 500$  ( $\lambda_1$  decreases from  $-0.00591$  to  $-0.01146$ ) to 2.3636 at  $Re = 2000$  ( $\lambda_1$  decreases from  $-0.00135$  to  $-0.00321$ ). The stabilizing effect of spanwise forcing is significant, since at  $Re = 2000$  the negative real part of the least-stable eigenvalue increases (in absolute value) by more than 2.3 times. It should come as no surprise that the effectiveness of the forcing depends on its amplitude  $A$ :

TABLE I. Largest relative increase  $R_{\text{mod}}$  of the modal stability margin, and the corresponding forcing parameters at which it is observed.

Re	$\kappa$	$\beta$	$A$	$R_{\text{mod}}$
500	2.25	0.7	1	1.9380
1000	2.00	0.5	1	2.1725
2000	3.00	0.5	1	2.3636

indeed, in Table I the largest  $R_{\text{mod}}$  are consistently obtained for the largest forcing amplitude tested, i.e.,  $A = 1$ . Once the optimal values of  $\kappa$  and  $\beta$  are determined, Fig. 4 depicts how  $R_{\text{mod}}$  changes as a function of  $A$ . For all Reynolds numbers studied,  $R_{\text{mod}}$  is quite similar to the turbulent drag reduction rate, and exhibits a monotonic growth from the uncontrolled case with  $R_{\text{mod}} = 1$ , then saturating at large amplitudes. Especially at higher Re, the effect of forcing is already noticeable at rather small forcing intensity: for example, at  $\text{Re} = 2000$  a forcing with  $A = 0.5$  provides more than 85% of the benefit achievable at  $A = 1$ . This observation is important in view of the rapid increase of the energetic cost of the forcing.

To examine how the results depend on  $\kappa$ , we first observe that, in Table I, the optimal  $\kappa$  does not vary much with Re. Indeed, the optimum with respect to  $\kappa$  is rather flat. As an example, at  $\text{Re} = 2000$ , Fig. 5 plots  $R_{\text{mod}}$  in  $A$ - $\beta$ -planes taken at three selected values of  $\kappa$ , namely,  $\kappa = 0.75$ ,  $\kappa = 2.75$ , and  $\kappa = 5$ . The plot demonstrates the weak dependence of  $R_{\text{mod}}$  on the forcing wave number, especially in the vicinity of the optimum value  $\kappa = 3$ .

### B. Nonmodal stability

To shed light on the forcing-induced modifications to the short-term stability properties of the flow, we now proceed to consider the transient growth function  $G(t)$  and its maximum  $G_{\text{max}}$ .  $G_{\text{max}}$  is the maximum possible relative amplification of the initial perturbation energy, occurring at time  $t_{\text{max}}$  for a specific initial condition referred to as the optimal input. We quantify the effect of the

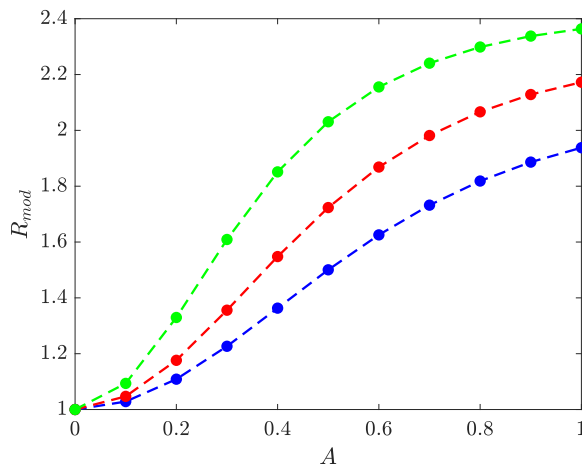


FIG. 4. Dependence of  $R_{\text{mod}}$  on the forcing amplitude  $A$  at optimal  $\kappa$  and  $\beta$  reported in Table I for  $\text{Re} = 500$  (blue),  $\text{Re} = 1000$  (red), and  $\text{Re} = 2000$  (green).

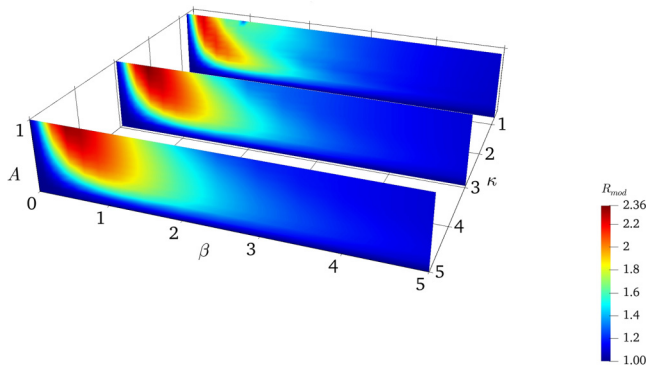


FIG. 5. Variation of  $R_{\text{mod}}$  at  $\text{Re} = 2000$  in three selected planes at  $\kappa = 0.75, 2.75, 5$ .

forcing on the nonmodal stability by computing the ratio  $R_{\text{nonmod}}$  defined as

$$R_{\text{nonmod}} = \frac{G_{\text{max}}^{\text{ref}}}{G_{\text{max}}},$$

where  $G_{\text{max}}^{\text{ref}}$  is the maximum transient growth for the reference Poiseuille flow. As in the modal analysis, the discretization parameters are set according to the criteria discussed in Appendix A. Table II presents the optimal parameters  $A$ ,  $\kappa$ , and  $\beta$ , which have been found to provide the largest  $R_{\text{nonmod}}$ . As for modal stability, changes in  $R_{\text{nonmod}}$  are Reynolds-number dependent, and the maximum reduction of the transient energy growth ranges from 65% at  $\text{Re} = 500$  (with  $G_{\text{max}}$  decreasing from 43.39 to 15.03) to 72% at  $\text{Re} = 2000$  (with  $G_{\text{max}}$  decreasing from 689.52 to 190.80).

At the optimal values ( $\kappa$ ,  $\beta$ ,  $A$ ) reported in Table II, the transient energy growth with and without forcing is compared in Fig. 6 (left). The transient growth is clearly inhibited by the spanwise forcing, and indeed the maximum energy amplification decreases from about 700 times the initial energy to less than 200 times; moreover, the maximum amplification occurs at an earlier time. At least for this specific case,  $G(t)$  for the forced case is above the reference curve for very short times.

The role of the two parameters  $A$  and  $\kappa$ , defining the wall forcing, is similar to the one discussed previously for modal stability. The forcing amplitude directly affects the amount of transient growth reduction, as clearly shown in Fig. 6 (right), while the forcing wave number  $\kappa$  has a lesser effect: as the wave number exceeds the optimal values identified in Table II (which are close to the minimum value of  $\kappa = 0.5$  considered in the present paper), the effectiveness of the forcing does not exhibit a significant or rapid decrease.

Nonmodal stability theory readily provides access to the shape of the perturbation that triggers the maximum transient energy growth. The optimal input (and the corresponding optimal output), discussed in Sec. II and obtained by means of a singular values decomposition, are examined in physical space in Figs. 7 and 8.

In particular, Fig. 7 describes how the optimal initial condition is affected by the forcing. The top row refers to the reference case with  $A = 0$  and confirms that, for plane Poiseuille flow, the

TABLE II. Largest decrease of the transient growth  $R_{\text{nonmod}}$  and corresponding forcing parameters.

Re	$\kappa$	$\beta$	$A$	$R_{\text{nonmod}}$
500	1.25	1.5	1	2.8877
1000	0.75	2.5	1	3.3670
2000	0.75	1.5	1	3.6140

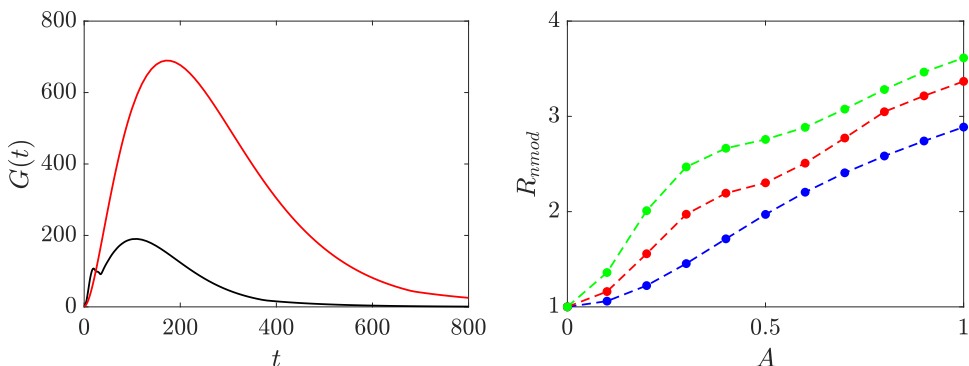


FIG. 6. Left: Transient energy growth  $G(t)$  for  $Re = 2000$  (black) for the optimal values of  $\beta = 1.5$  and  $\kappa = 0.75$ , compared to the unforced case (red). Right: Dependence of  $R_{nmod}$  on the forcing amplitude  $A$  for  $Re = 500$  (blue),  $Re = 1000$  (red), and  $Re = 2000$  (green).

optimal initial condition is a streamwise-constant pair of large-scale space-filling rolls. Indeed, in Fourier space such a perturbation is fully represented by the mode  $p = 0$ , leading to an effective streamwise wave number  $\alpha = 0$ . When the spanwise forcing is active with  $A = 1$  (bottom row), the optimal initial condition is characterized by different streamwise wave numbers. In particular, the morphology of the streamwise component of the optimal initial condition reveals the fundamental mode of the forcing, with superimposed higher harmonics. A striking difference to the unforced case is that the  $u$  component, although not entirely two-dimensional, is predominantly structured along the spanwise direction, i.e., orthogonal to the unforced case. Another significant difference is the fact that the perturbation becomes highly localized near the wall, and remains confined within the high-shear region produced by the spanwise Stokes layer described by the base flow. Though barely visible at this  $Re$ , a streamwise modulation can be observed in the spanwise component

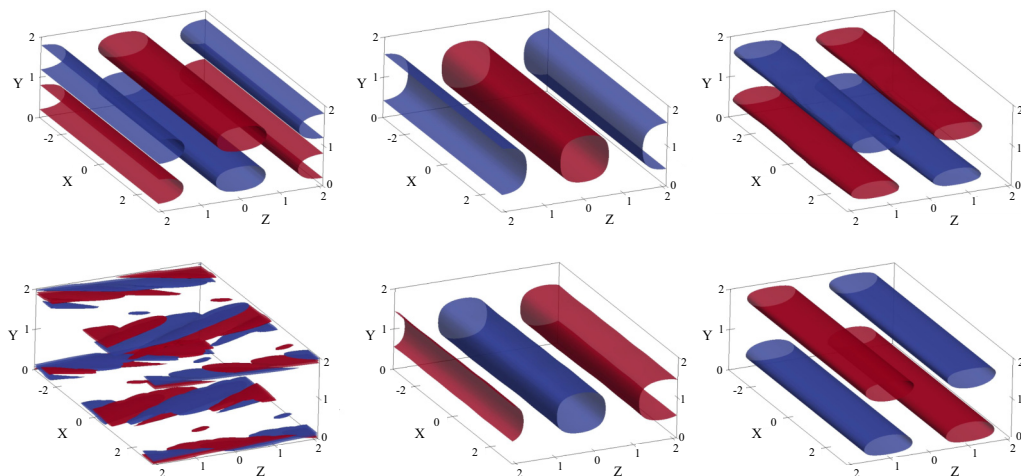


FIG. 7. Optimal initial condition computed for  $Re = 2000$ ,  $\kappa = 1$ , and  $\beta = 1.5$ : Unforced flow at  $A = 0$  (top) and forced flow at  $A = 1$  (bottom). For each velocity component ( $u$ ,  $v$ ,  $w$  from left to right), isosurfaces at  $\pm 60\%$  of their respective maxima are visualized. After normalizing the perturbation to unit maximum amplitude, the  $u$ ,  $v$ ,  $w$  components of the maximum are 0.11, 2.68, 3.79 for  $A = 0$ , and 0.74, 2.63, 3.79 for the  $A = 1$  case.

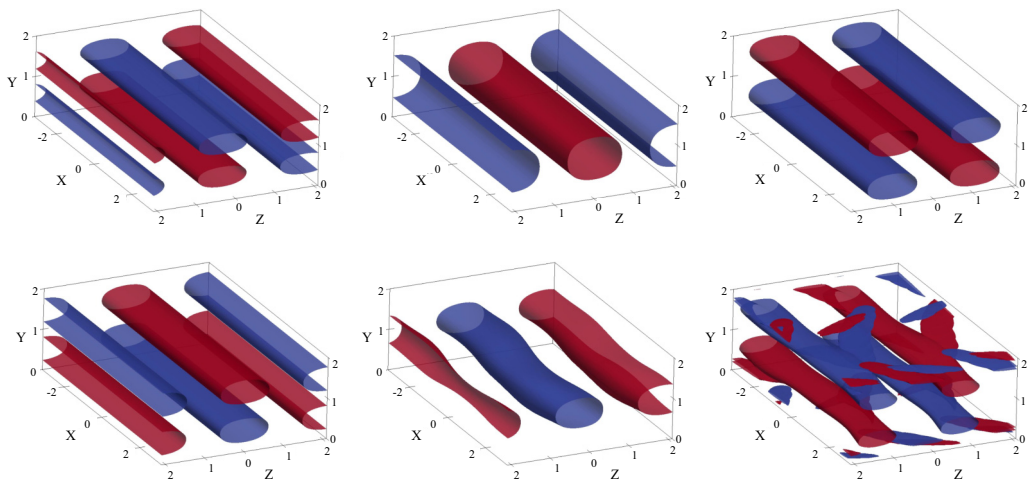


FIG. 8. Evolution of the optimal initial condition at the time of maximum energy growth, computed for  $Re = 2000$ ,  $\kappa = 1$ , and  $\beta = 1.5$ : Unforced flow at  $A = 0$  (top) and forced flow at  $A = 1$  (bottom). For each velocity component ( $u$ ,  $v$ ,  $w$  from left to right) isosurfaces at  $\pm 60\%$  of their respective maxima are visualized. The  $u$ ,  $v$ ,  $w$  components change by a factor of 481,0.47,0.40 for  $A = 0$ , and by a factor of 44,0.51,0.46 for  $A = 1$  with respect to the initial condition.

as well, whose overall shape, however, still resembles very much that of the unforced flow. The vertical component appears to be essentially unaffected by the forcing. In terms of relative intensity, the three velocity components are comparable with/without control; while the amplitudes of the wall-normal and spanwise components are unchanged, that of the longitudinal component, which is the smallest, grows by about six times in the controlled case.

If attention is drawn to the temporal evolution of the optimal initial condition, shown in Fig. 8 at the time of maximum energy amplification, similar effects are evident regarding its spatial shape; the spanwise forcing at the wall introduces a streamwise modulation with higher harmonic components. The modulation is, however, more reduced in comparison to the initial condition, and—at least for the case under consideration—it appears that at  $t = t_{\max}$  the perturbation has developed the same qualitative shape in both cases. The reorientation of the  $u$  component from the spanwise to the streamwise direction is attributed to an Orr-type mechanism [41]: the initial disturbance is characterized by a flow pattern opposed to the mean shear which, as time evolves, is tilted into the shear direction.

To explain how the transient growth is altered, one has to consider the energy levels of the perturbation. Within the present linear setting, the absolute value of the perturbation amplitude is inconsequential and perturbations are normalized to unit maximum absolute value. However, the relative values of the various components and their growth rates can be informative. In the reference flow, the three velocity components of the initial condition at  $Re = 2000$  are relatively balanced, but the transient growth affects them very differently. In fact, the relative increment of the amplitude of the streamwise component is 481 times the initial value (this figure is obviously Re-number dependent), whereas the  $v$  and  $w$  components decrease by factors of 0.47 and 0.46, respectively. With spanwise forcing, however, the picture is drastically changed. The evolution of the  $v$  and  $w$  components is similar to the unforced case, as they reduce to 0.51 and 0.46 of their initial values for  $v$  and  $w$ , respectively. However, the growth of the streamwise component is severely inhibited, and at  $t = t_{\max}$  the increase of the streamwise velocity component is only 44 times instead of 481 times.

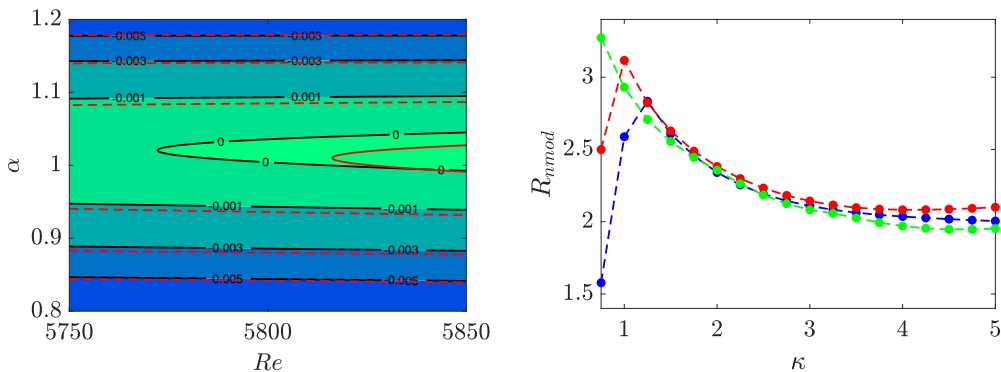


FIG. 9. Modal and nonmodal stability characteristics computed by taking  $\beta$  as a free parameter to select the worst case. Left: Neutral stability curves for the unforced flow (contour plot and black lines) and the forced flow (red lines) for  $A = 1$  and  $\kappa = 3$ . Right: Dependence of  $R_{\text{nmod}}$  on  $\kappa$  at  $A = 1$  and  $\text{Re} = 500$  (blue),  $\text{Re} = 1000$  (red), and  $\text{Re} = 2000$  (green).

### C. Discussion

The largest  $R_{\text{mod}}$  and  $R_{\text{nmod}}$  identified in this paper correspond to the best performance observed in the parameter space  $(A, \kappa, \beta)$  for a given  $\text{Re}$ . However, it is important to realize that the amplitude and wave number are indeed specifiable parameters of the forcing, but the spanwise wave number  $\beta$  of the perturbation, describing a generic small disturbance, is not a control parameter. Furthermore, background disturbances are realistically assumed to contain all frequencies. Hence, to appreciate the true potential of spanwise forcing, one should compare the neutral curve of the unmanipulated Poiseuille flow with a neutral curve for the controlled Poiseuille flow, where all values of  $\beta$  are considered and the worst-case scenario is selected. This is shown in Fig. 9 (left), where a forcing defined by  $\kappa = 3$  and  $A = 1$  is selected from the optimal parameters identified above. For the neutral curve, we scan through  $\text{Re}$  from 5750 to 5850 by increments of 5, and through the wave number  $\alpha$  from 0.8 to 1.2 by increments of 0.05. Every point in the  $\text{Re}$ - $\alpha$  plane for the forced flow results from a scan over all available spanwise wave numbers  $\beta$ . For the unforced flow, the critical value  $\text{Re}_c$  of the Reynolds number is the well-known  $\text{Re}_c = 5772$ ; for  $A = 1$ , this threshold is increased, but only marginally so, to  $\text{Re}_c = 5816$ . The increment is not particularly relevant, in contrast to the optimal situation discussed above in Sec. IV A. In line with the minimal change of  $\text{Re}_c$ , the shape of the most unstable eigenmode, i.e., the linearly unstable Tollmien–Schlichting wave, is also not altered significantly by the forcing. This means that the spanwise forcing is indeed capable of hindering the growth of certain spanwise perturbations, but not of all of them. Once the global effect of the forcing is considered in a scenario where perturbations of any wave number  $\beta$  are present, the improvement is significantly smaller.

However, in the context of highly subcritical flows, the significance of this result is limited, since the nonmodal stability characteristics are way more important. With nonmodal stability, the overall picture improves substantially. The maximum transient growth is significantly inhibited by spanwise forcing, regardless of the considered perturbation. As shown in Table II, the ratio  $R_{\text{nmod}} = G_{\text{max}}^{\text{ref}}/G_{\text{max}}$  increases from 2.89 at  $\text{Re} = 500$  to 3.61 at  $\text{Re} = 2000$ . Following the discussion above, it is interesting to assess how the forcing improves the stability characteristics by finding the value of  $\beta$  which yields the minimum  $R_{\text{nmod}}$ . Figure 9 (right) plots how  $R_{\text{nmod}}$  depends on  $\kappa$ , at  $A = 1$  and for the three Reynolds numbers, after selecting the  $\beta$  that yields the worst performance. Unlike the modal case, the beneficial effects of the spanwise forcing on the nonmodal stability characteristics are significant. Figure 9 (right) confirms again that, once  $\kappa$  remains at or above the optimal values, the forcing remains rather effective and consistently guarantees at least halving the transient energy growth, regardless of  $\text{Re}$  and the wave number of the spanwise perturbation.

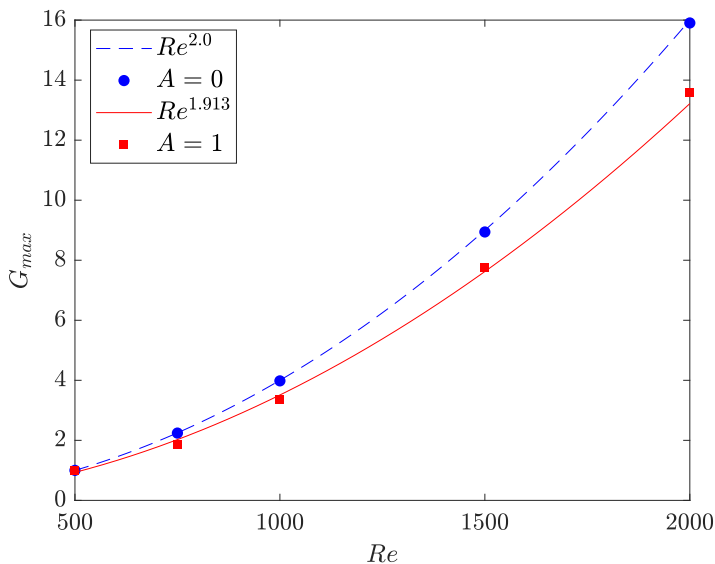


FIG. 10. Dependence of the maximum transient growth  $G_{\max}$  on the Reynolds number.

The case  $\beta = 0$  is the worst scenario only in the uncontrolled case; for each data point presented in Fig. 9, a comprehensive parametric study is conducted to determine the value of  $\beta$  that yields the worst modal/nonmodal improvement. Overall, the spanwise forcing appears to have little or no effect on the linearly unstable Tollmien–Schlichting waves detected by modal stability, but interacts favorably with the lift-up effect.

It is also interesting to explore in more detail how results depend on the Reynolds number. It is known [42] that the transient growth is a phenomenon whose dynamical importance increases with  $Re$ ; in particular, the maximum transient growth  $G_{\max}$  increases as  $Re^2$  for a canonical Poiseuille flow. When the flow is controlled by spanwise forcing, the  $Re$  dependence is similar but not identical, as shown in Fig. 10, which neatly confirms the  $Re^2$  increase for the case with  $A = 0$ , and shows for the controlled case a slightly slower increase, fitted well by the power law  $Re^{1.9}$ .

We conclude by mentioning the outcome of the same study repeated with the spanwise forcing applied to one wall only. It is confirmed that the control remains effective, but significantly less so compared to the case with forcing applied on both walls. For example, at  $Re = 2000$  and  $A = 1$ , i.e., the case depicted in Fig. 6, applying the control on both walls yields  $R_{\text{mod}} = 1.55$  and  $R_{\text{nmod}} = 3.61$ , which reduce to  $R_{\text{mod}} = 1.14$  and  $R_{\text{nmod}} = 1.37$  when a sole wall is activated. This is somewhat expected, since the flow dynamics over the two walls are decoupled, while the quantities  $R_{\text{mod}}$  and  $R_{\text{nmod}}$  refer to the entire volume; in other words, when control is applied to one wall only, instability is nearly unaffected on the other. This observation should not be overemphasized, though, as the fact that spanwise forcing remains fully effective in a boundary for both delaying transition and decreasing the friction drag is fully assessed [23,43].

## V. CONCLUDING DISCUSSION

The present paper explores the potential of a flow control technique, originally conceived for the reduction of skin-friction drag in the turbulent regime, to alter the linear stability characteristics of a wall-bounded shear flow. In the simplest geometry of a plane parallel channel, we have studied the modal and nonmodal temporal stability of laminar, pressure-driven Poiseuille flow modified by spanwise wall forcing. Specifically, the spanwise velocity enforced at the wall is steady, spanwise uniform, and sinusoidally modulated along the streamwise direction. A spanwise Stokes layer

develops, the SSL described by Viotti *et al.* (2009) [24]: Owing to the convective nature of Poiseuille flow, the steady forcing is effectively unsteady as seen by the convecting near-wall turbulence structures, and is known to provide large skin-friction drag reduction as well as interesting net energy savings in the turbulent regime.

The mathematical formulation of the stability problem is not straightforward, owing to the streamwise-varying base flow. The sinusoidal streamwise variations of the base flow is used to arrive at a formulation with a block-coupled system matrix. A numerical study has investigated a large number of parameters, both physical ( $Re$ ,  $A$ ,  $\kappa$ ,  $\beta$ ) and related to the numerical discretization ( $N$ ,  $M$ ,  $n_{\text{eig}}$ ,  $\Delta t$ ,  $T_{\text{end}}$ ). Overall, a total of 11 286 cases has been computed and processed. Special care has been taken to properly select the discretization parameters for discretization-independent solutions, while keeping the computational cost under control.

The main results fully support the finding that a turbulent skin-friction drag reduction technique can be employed to improve the stability characteristics of a laminar flow. In this respect, this conclusion reinforces similar results recently obtained numerically (see, e.g., Ref. [23]) in terms of transition delay. Looking at the asymptotic behavior of the perturbation (modal stability), the least stable eigenvalue  $\lambda_1$  has been found in our study to increase its stability margin in comparison to its Orr-Sommerfeld counterpart (Fig. 4), in a way that is directly related to the forcing intensity. Similarly, the potential for short-time growth of energy of small perturbations is significantly hampered in comparison to the unforced case. The relative stability improvements are  $Re$  dependent: When  $A = 1$ , across the tested values of the Reynolds number the real part of the least stable eigenvalue more than doubles, as shown in Table I: the ratio  $Re(\lambda_1)/Re(\lambda_1^{\text{ref}})$  increases from 1.94 at  $Re = 500$  to 2.36 at  $Re = 2000$ . The maximum energy growth decreases by 65% at  $Re = 500$  and by 72% at  $Re = 2000$ .

Further work is needed to improve our understanding of the whole picture and to approach applications, especially in terms of suitable actuators. Moreover, as generally observed for spanwise forcing, the obtained benefits are proportional to the forcing intensity, and at  $A = 1$  (maximum control velocity equal to the centerline velocity) the intensity is rather large. In the turbulent regime, this would lead to significant skin-friction drag reductions accompanied by negative net savings. The energetic convenience of the present forcing should be properly reassessed here, in view of the savings made possible by delayed transition. Nonetheless, the present results convincingly support the claim that spanwise forcing (at least in the stationary and spatially nonuniform case considered here) is an effective way to improve the linear stability characteristics of plane Poiseuille flow.

## ACKNOWLEDGMENTS

Preliminary results of this research were presented [44] at the XIII EUROMECH Turbulence Conference in Warsaw. Dr. C. Sovardi is thanked for his support work during his Master thesis.

The authors report no conflict of interest.

## APPENDIX: DISCRETIZATION PARAMETERS

For each set of physical parameters, the discretization parameters must be chosen. Some are simply set beforehand after a preliminary study, while others are dynamically adapted during the calculation on a case-by-case basis to consistently satisfy certain criteria across the whole study. In the following, we describe how the discretization parameters have been chosen to ensure consistent, high-fidelity solutions.

### 1. Number of Chebyshev polynomials

The number  $N$  of Chebyshev polynomials used to discretize the wall-normal direction must be sufficiently large to provide accurate values of the most unstable eigenvalues and of the maximum  $G_{\text{max}}$  of the function  $G(t)$ . For standard Poiseuille flow, ample literature is available (see, e.g.,

TABLE III. Modal and nonmodal stability results as a function of the number  $N$  of Chebyshev polynomials and of the forcing wave number  $\kappa$  for  $\text{Re} = 1000$ ,  $\beta = 1.5$ , and  $A = 1$ . Left: Real part of the least stable eigenvalue  $\lambda_1$  multiplied by  $10^2$ . Right: Maximum value  $G_{\max}$  of the transient energy growth function.

$\kappa$	$N = 40$	$N = 80$	$N = 100$	$N = 120$	$N = 40$	$N = 80$	$N = 100$	$N = 120$
0.5	-0.71597	-0.71589	-0.71589	-0.71589	89.2768	221.0830	236.2375	240.5213
0.75	-0.69655	-0.69662	-0.69662	-0.69662	56.6170	78.4394	80.0837	80.2476
1	-0.68968	-0.68974	-0.68974	-0.68974	53.1008	53.2548	53.2840	53.2953
1.5	-0.68762	-0.68745	-0.68745	-0.68745	63.3796	63.4602	63.4707	63.4793
2.5	-0.75017	-0.75032	-0.75032	-0.75032	67.9628	67.9501	67.9571	67.9720
3.5	-0.80562	-0.80556	-0.80556	-0.80556	66.5897	66.6047	66.6061	66.6080
5	-0.83934	-0.83936	-0.83936	-0.83936	65.7172	65.6933	65.6931	65.6934

Refs. [27,45–47]) to inform the choice of a suitable  $N$ ; here, however, the presence of an additional spanwise base flow calls for a further systematic analysis.

A preliminary resolution study is thus carried out for a typical case, with  $\text{Re} = 1000$ ,  $\beta = 1.5$ , and  $A = 1$ , where the wave number is varied from  $\kappa = 0.5$  to  $\kappa = 5$ . The effect of changing  $N$  is observed on the main modal and nonmodal stability characteristics: Table III reports on the left the real part of the least stable eigenvalue  $\lambda_1$ , and on the right the maximum value  $G_{\max}$  of the transient growth function.  $N$  is varied from  $N = 40$  to  $N = 120$ . The modal stability characteristics are weakly sensitive to the value of  $N$ , with  $N = 80$  already providing the first eigenvalue accurate up five digits regardless of the value of  $\kappa$ . The nonmodal results, however, show a strong dependence on  $N$ , especially for the lowest values of  $\kappa$ : When  $\kappa \geq 1$  the effects are minor, and  $N = 80$  provides  $G$  values that are stable to the fourth digit or higher. At lower  $\kappa$ , the accuracy degrades and the largest value of  $N = 120$  still does not provide resolution-independent results for  $\kappa = 0.5$ . Fortunately, as will be shown below, this case at the lowest  $\kappa$  shows changes in  $G_{\max}$  of less than 2% when moving from  $N = 100$  to  $N = 120$  and is of no practical interest. Moreover, the subsequent case with  $\kappa = 0.75$  displays far lower sensitivity to  $N$ , reduced by one order of magnitude.

The above considerations lead to our operational choice of using  $N = 80$  Chebyshev polynomials when  $\kappa \geq 1$ , but increasing this number to  $N = 100$  when  $\kappa < 1$ . The selected resolution is further checked on the most demanding situation, i.e., nonmodal stability calculations at the highest  $\text{Re}$  considered in the present paper ( $\text{Re} = 2000$ ). For  $N = 100$  polynomials, we compute a maximum transient growth at  $\kappa = 0.75$  of 190.8346, which is to be compared with a value of 190.8451 obtained with  $N = 120$  polynomials.

## 2. Truncation factor

The truncation factor  $M$  in Eqs. (12) defines the spectral expansion of the flow variables in the streamwise direction. The computed values of both  $\lambda_1$  and  $G_{\max}$  should be robust to the chosen value of  $M$ —a parameter which also strongly affects the computational cost.

Since in nonmodal stability analyses the optimal perturbation is not constrained to a single streamwise wave number,  $M$  should be sufficiently large to guarantee a compact support for the optimal initial condition, while also accurately capturing its evolution up to the time of maximum energy growth. We have empirically established that the optimal initial conditions obtained by varying the problem parameters can be grouped into two broad classes with qualitatively different characteristics in terms of spectral content. Figure 11 shows, for the two classes of optimal initial conditions, how their amplitude depends on the wall-normal coordinate  $y$  and on the modal expansion index  $p$ . In the first class (top row of Fig. 11), the  $v$  component is largest at  $\alpha = 0$ , i.e.,  $p = 0$ , whereas the  $\eta$  component is largest near the walls at  $\alpha \sim A/\kappa$ . In the second class (bottom row), both  $v$  and  $\eta$  show maxima at a wave number inversely proportional to  $\kappa$ . The temporal evolutions of perturbations from either class are qualitatively similar.

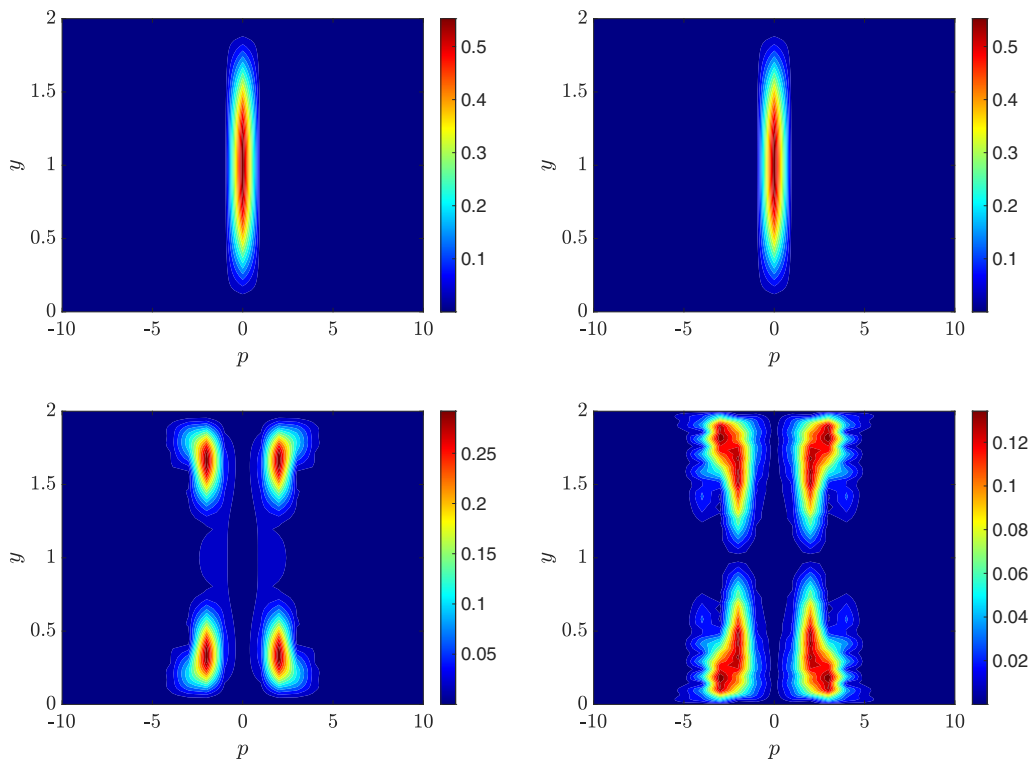


FIG. 11. Optimal initial condition at  $\text{Re} = 1000$  for  $v$  (left) and  $\eta$  (right) as a function of the  $y$  coordinate and the  $p$ th wave number of the modal expansions,  $-M \leq p \leq M$ . Contours describe the absolute value of the optimal initial condition. Top: Example of optimal input centered around  $p = 0$ , with  $\kappa = 1.5$ ,  $A = 0.3$ , and  $\beta = 0.5$ . Bottom: Example of optimal input peaking at  $\alpha \sim \pm\kappa^{-1}$  with  $\kappa = 1$ ,  $A = 0.6$ , and  $\beta = 0.3$ .

Owing to the procedural complexity of properly selecting the parameter  $M$ , our operational choice is to enforce a dynamical and automated adjustment of  $M$ . Each simulation is started with a reasonable first guess  $M_0$ , and then  $M$  is incremented by unitary steps until a most unstable eigenvalue  $\lambda_1^M$  is computed that satisfies the criterion

$$\left| \frac{\lambda_1^M - \lambda_1^{M-1}}{\lambda_1^M} \right| < 1 \times 10^{-6}. \quad (\text{A1})$$

The initial guess  $M_0$  is selected by empirically accounting for the two distributions discussed above, according to the following heuristics that depends on the forcing parameters:

$$M_0 = 3 \frac{A}{\kappa} + \frac{1}{\kappa}. \quad (\text{A2})$$

Once  $M_0$  is set, an iterative increase of  $M$  is started until the termination criterion Eq. (A1) is satisfied (or a maximum value of  $M_{\max} = 50$  is reached). Across the entire study, this iteration always terminated before the limit  $M = M_{\max}$  is reached, and the largest value used within our study was  $M = 18$ .

Provided that  $M$  is not too low, the values of  $G_{\max}$  are not particularly sensitive to  $M$ , as shown in Table IV. For this case, our procedure leads to  $M = 11$ , and the relative change of  $G_{\max}$  for values of  $M$  between  $M = 11$  and  $M = 18$  is bounded by  $10^{-3}$ .

TABLE IV. Nonmodal stability results as a function of the modal truncation factor  $M$  for  $\text{Re} = 2000$ ,  $\kappa = 0.75$ ,  $\beta = 2$  and  $A = 1$ .

$M$	8	10	11	14	18
$G_{\max}$	231.1303	231.1788	231.2086	231.2300	231.2390

### 3. Number of eigenvalues

The fraction of the entire set of  $N_{\text{tot}} = 2(N + 1)(2M + 1)$  eigenvalues of the system matrix retained in the iterative Arnoldi procedure must ensure that the dynamics of the optimal initial condition is well represented. The number  $n_{\text{eig}}$  of retained eigenvalues defines the truncation operator  $\mathbf{T}$ , which reduces the size of the matrix  $\mathbf{Q}_s$  and with it the cost of computing the transient growth rate Eq. (22).

The worst-case scenario corresponds to optimal initial conditions of the type illustrated in the bottom row of Fig. 11. For one such case (namely,  $\text{Re} = 1000$ ,  $A = 0.6$ , and  $\beta = 0.3$ ), Table V reports the computed value of  $G_{\max}$  as  $n_{\text{eig}}$  is changed, for selected values of  $\kappa$ . The sensitivity is certainly nonnegligible, especially at the lower  $\kappa$ . By examining this case as well as other representative cases, we arrive at the operational choice of setting  $n_{\text{eig}} = N_{\text{tot}}/6$  when  $\kappa \geq 1$ , and  $n_{\text{eig}} = N_{\text{tot}}/3$  otherwise.

### 4. Temporal discretization

A temporal integration step  $\Delta t$  must be chosen to evaluate Eq. (22) and to identify the maximum  $G_{\max}$  and the time  $t_{\max}$  at which it occurs. In classic, unforced Poiseuille flow, the transient growth function  $G(t)$  monotonically increases from a unit value at  $t = 0$  (as long as  $\text{Re}$  is above the critical value for monotonic stability) up to  $G_{\max}$ , and then steadily decreases. However, when the flow is modified by the SSL, the ensuing  $G(t)$  presents two local maxima: one is similar to the unforced maximum, the other is directly linked to the SSL. The latter is centered on a considerably narrow peak of the  $G(t)$  function, and typically occurs at shorter times. The absolute maximum  $G_{\max}$  can pertain to either peak, depending on the specific case.

The location of the two peaks varies significantly with the physical parameters of the problem. Figure 12 shows, for a typical case with dominating first peak ( $\text{Re} = 1000$  and  $\kappa = 1$ ), the temporal position of the peak as a function of  $A$  and  $\beta$ . It is seen that, especially at small  $\beta$ ,  $G_{\max}$  occurs at very short times, whereas for small  $A$  the timescale of the maximum increases, and the unforced peak is recovered. It is also noted that the first peak of  $G(t)$  is always located at  $t < 100$ . Hence our operational choice is to employ a variable time discretization by setting  $\Delta t = 1$  for  $0 < t < 100$  and increasing it to  $\Delta t = 10$  for  $t > 100$ .

 TABLE V. Nonmodal stability results as a function of the number  $n_{\text{eig}}$  of eigenvalues retained in the Arnoldi procedure and of the forcing wave number. The table reports the maximum value of the transient energy growth function  $G(t)$ .

$\kappa \backslash n_{\text{eig}}$	$N_{\text{tot}}/7$	$N_{\text{tot}}/6$	$N_{\text{tot}}/5$	$N_{\text{tot}}/4$	$N_{\text{tot}}/3$	$N_{\text{tot}}/2$
0.5	20.2629	20.7811	20.8603	20.8655	20.8657	20.8657
0.75	15.0971	15.1162	15.1261	15.1266	15.1266	15.1266
1	13.1278	13.1681	13.1957	13.2004	13.2013	13.2015
1.5	12.4396	12.4427	12.4431	12.4432	12.4433	12.4437
2.5	10.0582	10.0583	10.0584	10.0585	10.0588	10.0590
3.5	10.4932	10.4934	10.4937	10.4938	10.4941	10.4943
5	10.9079	10.9081	10.9084	10.9084	10.9087	10.9089

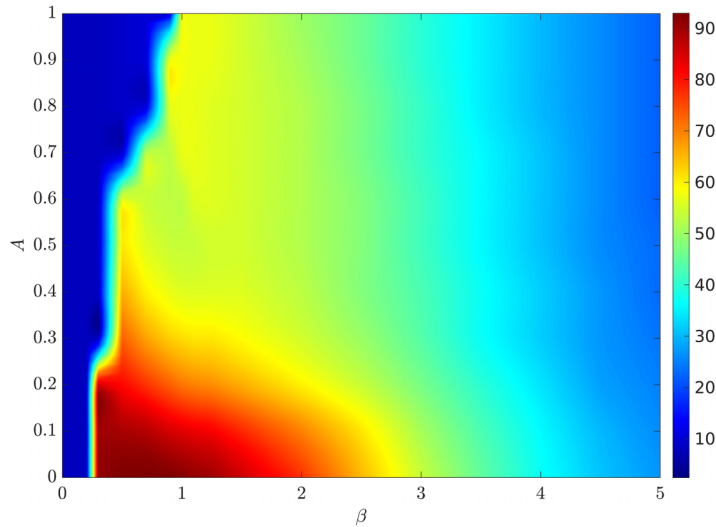


FIG. 12. Time  $t_{\max}$  for the occurrence of the maximum  $G_{\max}$  of transient growth for the case of  $Re = 1000$  and  $\kappa = 1$ .

- 
- [1] M. Quadrio, P. Ricco, and C. Viotti, Streamwise-traveling waves of spanwise wall velocity for turbulent drag reduction, *J. Fluid Mech.* **627**, 161 (2009).
  - [2] M. Quadrio, Drag reduction in turbulent boundary layers by in-plane wall motion, *Philos. Trans. R. Soc. London A* **369**, 1428 (2011).
  - [3] M. A. Leschziner, Friction-drag reduction by transverse wall motion—a review, *J. Mech.* **36**, 649 (2020).
  - [4] P. Ricco, M. Skote, and M. A. Leschziner, A review of turbulent skin-friction drag reduction by near-wall transverse forcing, *Prog. Aeronaut. Sci.* **123**, 100713 (2021).
  - [5] M. Quadrio and P. Ricco, Critical assessment of turbulent drag reduction through spanwise wall oscillation, *J. Fluid Mech.* **521**, 251 (2004).
  - [6] J. Banchetti, P. Luchini, and M. Quadrio, Turbulent drag reduction over curved walls, *J. Fluid Mech.* **896**, A10 (2020).
  - [7] M. Quadrio, A. Chiarini, J. Banchetti, D. Gatti, A. Memmolo, and S. Pirozzoli, Drag reduction on a transonic airfoil, *J. Fluid Mech.* **942**, R2 (2022).
  - [8] A. Yakeno, Drag Reduction and transient growth of a streak in a spanwise wall-oscillatory turbulent channel flow, *Phys. Fluids* **33**, 065122 (2021).
  - [9] F. Auteri, A. Baron, M. Belan, G. Campanardi, and M. Quadrio, Experimental assessment of drag reduction by traveling waves in a turbulent pipe flow, *Phys. Fluids* **22**, 115103/14 (2010).
  - [10] I. Marusic, D. Chandran, A. Rouhi, M. K. Fu, D. Wine, B. Holloway, D. Chung, and A. J. Smits, An energy-efficient pathway to turbulent drag reduction, *Nat. Commun.* **12**, 5805 (2021).
  - [11] K. Gouder, M. Potter, and J. F. Morrison, Turbulent friction drag reduction using electroactive polymer and electromagnetically driven surfaces, *Exp. Fluids* **54**, 1441 (2013).
  - [12] D. Gatti, A. Güttler, B. Frohnäpfel, and C. Tropea, Experimental assessment of spanwise-oscillating dielectric electroactive surfaces for turbulent drag reduction in an air channel flow, *Exp. Fluids* **56**, 110 (2015).
  - [13] J. Bird, M. Santer, and J. F. Morrison, Experimental control of turbulent boundary layers with in-plane travelling waves, *Flow, Turbul. Combust.* **100**, 1015 (2018).
  - [14] M. R. Jovanović, Turbulence suppression in channel flows by small amplitude transverse wall oscillations, *Phys. Fluids* **20**, 014101 (2008).

- [15] P. Ricco, Laminar streaks with spanwise wall forcing, *Phys. Fluids* **23**, 064103 (2011).
- [16] S. M. E. Rabin, C. P. Caulfield, and R. R. Kerswell, Designing a more nonlinearly stable laminar flow via boundary manipulation, *J. Fluid Mech.* **738**, R1 (2014).
- [17] M. J. P. Hack and T. A. Zaki, The continuous spectrum of time-harmonic shear layers, *Phys. Fluids* **24**, 034101 (2012).
- [18] M. J. P. Hack and T. A. Zaki, The influence of harmonic wall motion on transitional boundary layers, *J. Fluid Mech.* **760**, 63 (2014).
- [19] M. J. P. Hack and T. A. Zaki, Modal and non-modal stability of boundary layers forced by spanwise wall oscillations, *J. Fluid Mech.* **778**, 389 (2015).
- [20] Y. Wang and C. Liu, Liutex (vortex) cores in transitional boundary layer with spanwise-wall oscillation, *J. Hydrodyn.* **31**, 1178 (2019).
- [21] C. A. Duque-Daza, M. F. Baig, D. A. Lockerby, S. I. Chernyshenko, and C. Davies, Modelling turbulent skin-friction control using linearised Navier-Stokes equations, *J. Fluid Mech.* **702**, 403 (2012).
- [22] P. S. Negi, M. Mishra, and M. Skote, DNS of a single low-speed streak subject to spanwise wall oscillations, *Flow, Turbul. Combust.* **94**, 795 (2015).
- [23] P. S. Negi, M. Mishra, P. Schlatter, and M. Skote, Bypass transition delay using oscillations of spanwise wall velocity, *Phys. Rev. Fluids* **4**, 063904 (2019).
- [24] C. Viotti, M. Quadrio, and P. Luchini, Streamwise oscillation of spanwise velocity at the wall of a channel for turbulent drag reduction, *Phys. Fluids* **21**, 115109 (2009).
- [25] J. M. Floryan, Stability of wall-bounded shear layers in the presence of simulated distributed roughness, *J. Fluid Mech.* **335**, 29 (1997).
- [26] J. Szumbariski and J. M. Floryan, Transient disturbance growth in a corrugated channel, *J. Fluid Mech.* **568**, 243 (2006).
- [27] P. J. Schmid and D. S. Henningson, *Stability and Transition in Shear Flows* (Springer-Verlag New York, Inc., New York, 2001).
- [28] M. Quadrio and P. Ricco, The laminar generalized stokes layer and turbulent drag reduction, *J. Fluid Mech.* **667**, 135 (2011).
- [29] M. Abramowitz and I. A. Stegun, *Handbook of Mathematical Functions*, Applied Mathematics Series, Vol. 55 (United States Department of Commerce, National Bureau of Standards (NBS), 1964).
- [30] J. P. Boyd, *Chebyshev and Fourier Spectral Methods*. 1st. ed (Springer-Verlag, Berlin, Heidelberg, 1989).
- [31] C. Canuto, M. Y. Hussaini, A. Quarteroni, and T. A. Zang, *Spectral Methods: Fundamentals in Single Domains* (Springer, Berlin, Heidelberg, 2006).
- [32] C. Canuto, M. Y. Hussaini, A. Quarteroni, and T. A. Zang, *Spectral Methods: Evolution to Complex Geometries and Applications to Fluid Dynamics* (Springer, Berlin, Heidelberg, 2007).
- [33] L. N. Trefethen and D. I. Bau, *Numerical Linear Algebra* (SIAM (Society for Industrial and Applied Mathematics), Philadelphia, 1997).
- [34] S. C. Reddy and D. S. Henningson, Energy growth in viscous channel Flows, *J. Fluid Mech.* **252**, 209 (1993).
- [35] W. O. Criminale and T. L. Jackson, *Theory and Computation of Hydrodynamic Stability* (Cambridge University Press, Cambridge, 2003).
- [36] C. W. Clenshaw and A. R. Curtis, A method for numerical integration on an automatic computer, *Numer. Math.* **2**, 197 (1960).
- [37] J. P. Imhof, On the method for numerical integration of Clenshaw and Curtis, *Numer. Math.* **5**, 138 (1963).
- [38] A. Hanifi, P. Schmid, and D. Henningson, Transient growth in compressible boundary layer flow, *Phys. Fluids* **8**, 826 (1996).
- [39] K. Maleknejad and T. Lotfi, Numerical expansion methods for solving integral equations by interpolation and Gauss quadrature rules, *Appl. Math. Comput.* **168**, 111 (2005).
- [40] P. Luchini and M. Quadrio, A low-cost parallel implementation of direct numerical simulation of wall turbulence, *J. Comput. Phys.* **211**, 551 (2006).
- [41] W. M. F. Orr, The stability or instability of the steady motions of a perfect liquid and of a viscous liquid. Part II. A viscous liquid, *Proc. R. Irsh. Acad. Sect. A: Math. Phys. Sci.* **27**, 69 (1907).
- [42] P. Schmid, Nonmodal stability theory, *Annu. Rev. Fluid Mech.* **39**, 129 (2007).

- [43] M. Skote, M. Mishra, and Y. Wu, Wall oscillation induced drag reduction zone in a turbulent boundary layer, [Flow, Turbul. Combust.](#) **102**, 641 (2019).
- [44] F. Martinelli, M. Quadrio, and P. J. Schmid, Linear stability of Poiseuille flow over the generalized Stokes layer, *Euromech Turbulence Conference XIII, Warsaw (PL), Sept. 12-15, 2011* (2011).
- [45] S. A. Orszag, Accurate solution of the Orr-Sommerfeld stability equation, [J. Fluid Mech.](#) **50**, 689 (1971).
- [46] S. C. Reddy, P. J. Schmid, and D. S. Henningson, Pseudospectra of the Orr-Sommerfeld operator, [SIAM J. Appl. Math.](#) **53**, 15 (1993).
- [47] A. J. Harfash, Numerical methods for solving some hydrodynamic stability problems, [Int. J. Appl. Comput. Math.](#) **1**, 293 (2015).